Transfer Function Analysis of a Surface Coupled Atomic Force Microscope Cantilever System

Rafael Vazquez, F.-J. Rubio-Sierra and Robert W. Stark

Abstract— Current methods to study atomic force microscope (AFM) cantilever dynamics use model simplification, or are based on the non-trivial solutions of the equation of motion. As an alternative method, transfer function analysis gives a complete description of system dynamics. In this work, we derive the exact, analytical expression for the multivariable infinite dimensional transfer function of a surface coupled cantilever system. The inputs of the system are punctual force at the tip end and distributed force along the cantilever, whereas the outputs are the position and slope at the tip end. A linearization of the surface coupling force is considered. Free cantilever and pinned end are considered as limit cases of the surface coupling. Frequency response Bode plots are shown, and transfer function infinite product expansion are obtained, which allow to derive the exact location of poles and zeros of the system, as a function of the level of surface coupling. This is shown in a root locus kind of plot. Transfer function analysis gives insight into optimal input/output configurations of the system and enables the possibility of model-based AFM operation.

I. INTRODUCTION

Since its invention in 1986 [2], the atomic force microscope (AFM) has played an important role in many scientific and technological applications. As a microscope, the AFM is not only capable of high-resolution surface imaging, but it can also obtain local quantitative material properties [4]. It can be used as well as a tool for manipulation at the nanoscale [18]. Due to its versatility, the AFM offers many different possibilities for surface modification [12].

Many efforts have been made to model the dynamics of the AFM cantilever. The simplest one consists in modelling the cantilever as a single degree of freedom harmonic oscillator [1], the so-called first mode approximation (FMA). However, even though the FMA is an useful approximation which can be used, for example, for state estimation [15], it neglects the fact that the cantilever is a distributed parameter system with an infinite number of resonant frequencies. This can be taken into account, including more modes through the use of a lumped-parameter model [17]. However, if damping or tip-sample interaction are included, the solution of the problem is not trivial [5], [9], [11]. A possible solution is to consider the full infinite dimensional system. The transfer functions of such systems consist in transcendental functions; therefore, in order to obtain system poles and zeros, infinite

R. Vazquez is with the Department of Mechanical and Aerospace Engineering, University of California San Diego, La Jolla, CA 92093-0411.

F. J. Rubio-Sierra and R. W. Stark are with the CeNS and Section Crystallography in the Dept. of Earthvand Environmental Sciences at the University of Munich. Theresienstr. 41, 80333 Munich, Germany (phone: +49 89 2180 4328, fax: +49 89 2180 4334; e-mail: rubio@lrz.uni-muenchen.de, stark@lmu.de)

product expansions must be used [7]. This kind of exact analysis has been applied before to study implications in modelling and control design of system configurations in flexible systems [16]. In [13] we performed such an analysis for the AFM without surface coupling.

We expand the analysis in [13] by considering a model with (linearized) variable surface coupling, which includes the free end as a limit case, as well as pinned end. This approach has been taken before for an undamped model [11], or lumped parameter model [17], but a complete system-theoretic description of the infinite dimensional damped model, including frequency responses and pole/zero location analysis, has not yet been done, to the best of our knowledge.

The paper is organized as follows. In Section II we present the input/output AFM system under consideration. Section III describes the surface coupling model we employ. In Section IV we introduce the AFM model and solve it using Laplace transform methods. This allows us to derive an analytic expression for the transfer function of the system, which we discuss in Section V, where some Bode plots are shown for a set of numerical values of the parameters. We also discuss the limit cases of free end and pinned end. Then, poles and zeros of the system are discussed in Sections VI and VII, respectively, where we plot a root locus diagram, showing how location of both poles and zeros change with the level (and sign) of surface coupling. We finish the paper with a discussion of the results in Section VIII.

II. AFM CANTILEVER SYSTEM

The AFM cantilever system under consideration has constant section, so it can be considered one-dimensional. The height of the cantilever will be described by the variable $z(t,x)$ defined positive for a displacement toward the sample, where t is time, $x \in [0, L]$ the position, and L is the length of the cantilever. $x = 0$ is the fixed end of the cantilever, and $x = L$ the tip end. The inputs and outputs of the system under consideration are the following:

- Input 1, $q(t)$, is the force acting at the tip end of the cantilever. This can be implemented by using a magnetic particle attached at the tip end, which is then actuated by generating a magnetic field [6].
- Input 2, $u(t)$, is a distributed force per unit length acting along the cantilever, which corresponds to the inertial forces generated by a base driven cantilever [19] or to an electrostatic force.
- Output 1, $z(t, L)$, is the position of the tip end of the cantilever, measurable by interferometric methods.

Usually this measurement is not available in commonly found AFM systems [14].

- Output 2, $z_x(t, L)$, is the slope at the tip end of the cantilever, which is measured using the bouncing beam detection method [10].

Considering the cantilever as a MIMO system, we can write its (matrix) transfer function description as

$$\begin{bmatrix} Z(s, L) \\ Z_x(s, L) \end{bmatrix} = G(s) \begin{bmatrix} U(s) \\ Q(s) \end{bmatrix}, \tag{1}$$

where the capital letters refer to Laplace transformed variables, s is the Laplace variable, and $G(s)$ is the matrix transfer function of the system,

$$G(s) = \begin{pmatrix} g_{11} & g_{12} \\ g_{21} & g_{22} \end{pmatrix}. \tag{2}$$

Here, $g_{ij}(s)$ is the transfer function of input i to output j.

III. TIP-SURFACE INTERACTION

The surface interaction force acting on the tip of the cantilever is a nonlinear function that depends mainly on the proximity of the tip to the sample [3]. Calling z_s the distance from the sample to the tip of the undeflected cantilever, $f(t)$ the force, and a_0 the interatomic distance, one can characterize two regimes . If $z_s - z(t, L) \geq a_0$, the force is attractive and can be described by a Van der Waals model,

$$f(t) = -\frac{HR}{6(z_s - z(L, t))^2}. \tag{3}$$

If $z_s - z(t, L) \leq a_0$, the interaction is repulsive and can be computed using a Derjaguin-Muller-Toporov (DMT) model,

$$f(t) = -\frac{HR}{6a_0^2} + \frac{4}{3} E^* \sqrt{R}(z_s - z(L, t) + a_0)^{3/2}. \tag{4}$$

In expressions (3)–(4), H represents the Hamaker constant, R the tip radius, and E^* the effective constant stiffness, which can be derived from the elastic moduli of tip and sample (respectively E_t and E_s) and their Poisson ratios (resp. ν_t and ν_s), using the following expression: $E^* = [(1 - \nu_t^2)/E_t + (1 - \nu_s^2)/E_s]^{-1}$.

We consider that the system stays in a small enough neighborhood of the equilibrium set point z_0, which can be adjusted moving the sample relative to the cantilever mount [11]. Linearizing the force around z_0, we obtain

$$f(t) = -k_{ts} z(t, L), \tag{5}$$

where k_{ts} represents the "contact stiffness", an effective spring contact defined as

$$k_{ts} = -\left. \frac{\partial f(t)}{\partial z(t, L)} \right|_{z_0}. \tag{6}$$

Plugging (3)–(4) into (5),

$$k_{ts} = \begin{cases} -\frac{HR}{3(z_s - z_0)^3}, & \text{if } z_s - z(t, L) \geq a_0, \\ 2E^* \sqrt{R(z_s - z_0 + a_0)}, & \text{if } z_s - z(t, L) \leq a_0. \end{cases} \tag{7}$$

Note that the sign of k_{ts} depends on the regime of the force. For the attractive regime one has a negative constant, while for the repulsive regime the constant is positive. We write

$$k_{ts} = \frac{3EI}{L^3} \hat{k}_{ts}, \tag{8}$$

where EI is the flexural stiffness and the quantity $3EI/L^3$ represents the cantilever spring constant. Then, $\hat{k}_{ts}$ is the parameter that determines the magnitude and regime of the force. In this work we consider all possible values of $\hat{k}_{ts}$ including zero (free end) and infinity (pinned end).

IV. DYNAMIC MODEL OF THE COUPLED SYSTEM

A mathematical model of the AFM system including the interaction force can be derived from the classical Euler-Bernouilli beam equation, in which we neglect rotary inertia, axial effects, shear deformation and tip mass, but include damping effects,

$$EI \frac{\partial^4 z}{\partial x^4} + c \frac{\partial z}{\partial t} + m \frac{\partial^2 z}{\partial t^2} = -u(t), \tag{9}$$

where EI corresponds to the flexural stiffness, c to the damping due to viscous friction, and m to the mass per unit length. The boundary conditions at the fixed end are

$$z(t, 0) = 0, \quad \left. \frac{\partial z}{\partial x} \right|_{x=0} = 0, \tag{10}$$

and at the tip end

$$\left. \frac{\partial^2 z}{\partial x^2} \right|_{x=L} = 0, \quad EI \left. \frac{\partial^3 z}{\partial x^3} \right|_{x=L} + f(t) = -q(t). \tag{11}$$

We have included the interaction force $f(t)$ and the input $q(t)$. Introducing the linearized force (5)–(8) in (11) yields

$$EI \left(\left. \frac{\partial^3 z}{\partial x^3} \right|_{x=L} - \frac{\hat{k}_{ts}}{3L^3} z(L, t) \right) = -q(t). \tag{12}$$

Following [13], we take Laplace transform and seek a solution[1]

$$\begin{aligned} Z(s, x) = & \cosh(\lambda(s)x) \left[A \cos(\lambda(s)x) + B \sin(\lambda(s)x) \right] \\ & + \sinh(\lambda(s)x) \left[C \cos(\lambda(s)x) + D \sin(\lambda(s)x) \right] \\ & + \frac{U(s)}{4EI\lambda(s)^4}, \end{aligned} \tag{13}$$

where

$$\lambda(s) = \sqrt[4]{\frac{cs + ms^2}{4EI}}. \tag{14}$$

The constants A, B, C, and D can be found by substitution in (10)–(11). Once the solution $Z(s, x)$ is found, the slope is obtained as $Z_x(s, x) = \partial Z / \partial x$. We skip the long analytic expression for the solution for the sake of clarity.

For numerical calculations and plots, we have employed the following numerical data extracted from [13]: $E = 179\,\text{GPa}$, $I = 3.64 \times 10^{-22}\,\text{m}^4$, $m = 4.08 \times 10^{-7}\,\text{kg/m}$, $L = 225\,\mu\text{m}$, and $c = 0.01\,\text{kg/ms}$. In the sequel, we omit the dependence on the Laplace variable s for clarity.

---

[1]The standard Euler-Bernouilli equations has a unique and regular solution. As it seems reasonable both mathematically and physically, we assume uniqueness also holds when adding the linearized interaction force. This could be false for the nonlinear model of the force.

V. TRANSFER FUNCTIONS

The matrix transfer function of the system, G, as defined in (1)–(2) can be found by evaluating the solutions $Z(x)$ and $Z_x(x)$ at $x = L$. Its expression is

$$G = \frac{1}{D} \left(\begin{array}{cc} n_{11} & n_{12} \\ n_{21} & n_{22} \end{array} \right), \qquad (15)$$

where the common denominator D is

$$\begin{aligned} D &= EI(2[2 + \cos(2\lambda L) + \cosh(2\lambda L)] \\ &\quad + \frac{3\hat{k}_{ts}}{L^3\lambda^3}[\sinh(2\lambda L) - \sin(2\lambda L)]), \end{aligned} \qquad (16)$$

and the value of the numerators is

$$n_{11} = \frac{1}{\lambda^3}[\sinh(2\lambda L) - \sin(2\lambda L)], \qquad (17)$$

$$n_{12} = \frac{1}{\lambda^2}[\cosh(2\lambda L) - \cos(2\lambda L)], \qquad (18)$$

$$n_{21} = \frac{-1}{2\lambda^4}[\cos(\lambda L) - \cosh(\lambda L)]^2, \qquad (19)$$

$$\begin{aligned} n_{22} &= \frac{-2}{\lambda^3}[\cosh(\lambda L)\sin(\lambda L) - \cos(\lambda L)\sinh(\lambda L)] \\ &\quad + \frac{3\hat{k}_{ts}}{2L^3\lambda^6}[\sin(\lambda L) - \sinh(\lambda L)]^2. \end{aligned} \qquad (20)$$

Note that only D and n_{22} depend on $\hat{k}_{ts}$.

We study each subsystem g_{ij} separately. Bode plots are shown in Fig. 1 for values $\hat{k}_{ts} = -1, 0, 10, 100$. The most interesting qualitative feature of the plots is the attenuation and displacement of resonant modes to the right, as $\hat{k}_{ts}$ increases, except in the most complex case of g_{22}, which we study in more detail in Sections VI and VII by characterizing the location of its poles and zeros. Also, in some cases there are modes of resonance that get strongly attenuated, almost disappearing or exchanging its position with one anti-resonance. This is the effect of an (stable) pole-zero cancellation that happens for a close value of $\hat{k}_{ts}$, and may change dramatically the behavior of the system in some frequency ranges. In the Bode plots, we do not show the frequency response for $\hat{k}_{ts} < -1$, since that range of values is shown in Section VI to lead to an unstable system.

A. Limit cases

There are two limit cases, when $\hat{k}_{ts} = 0$ and $\hat{k}_{ts} \to \infty$; the first case corresponds to a freely oscillating cantilever, and the second corresponds to a cantilever whose tip is "glued" to the surface (pinned), so the cantilever end $x = L$ is fixed. The expressions for these special cases are

$$G^0 = \lim_{\hat{k}_{ts} \to 0} G = \frac{1}{D^0} \left(\begin{array}{cc} n_{11} & n_{12} \\ n_{21} & n_{22}^0 \end{array} \right), \qquad (21)$$

and

$$G^\infty = \lim_{\hat{k}_{ts} \to \infty} G = \frac{1}{D^\infty} \left(\begin{array}{cc} 0 & 0 \\ 0 & n_{22}^\infty \end{array} \right), \qquad (22)$$

where

$$D^0 = 2EI\left(2 + \cos(2\lambda L) + \cosh(2\lambda L)\right), \qquad (23)$$

$$n_{22}^0 = \frac{-2}{\lambda^3}(\cosh(\lambda L)\sin(\lambda L) - \sinh(\lambda L)\cos(\lambda L)), \qquad (24)$$

$$D^\infty = \frac{2EI}{L^3\lambda^3}\left(\sinh(2\lambda L) - \sin(2\lambda L)\right), \qquad (25)$$

$$n_{22}^\infty = \frac{1}{L^3\lambda^6}\left(\sin(\lambda L) - \sinh(\lambda L)\right)^2. \qquad (26)$$

The freely vibrating cantilever (21) has been profusely studied, see [13] and references therein. We included it for the sake of completeness. The Bode plot of the second case is shown for the only nonzero component of G^∞ in (22), i.e., $g_{22}^\infty = n_{22}^\infty/D^\infty$, in Fig. 2.

VI. POLES

The poles, common to all subsystems, are the roots of the denominator D in (16). It is possible to explicitly find these roots by expressing the denominator as an infinite product. One must distinguish three cases depending on $\hat{k}_{ts}$.

1) If $\hat{k}_{ts} > -1$, then

$$D = C \prod_{n=1}^{\infty} \left[1 + \frac{4L^4\lambda^4}{d_n^4} \right]. \qquad (27)$$

2) If $\hat{k}_{ts} = -1$, then a root at zero must be added to (27),

$$D = \frac{88}{35}L^4\lambda^4 \prod_{n=1}^{\infty} \left[1 + \frac{4L^4\lambda^4}{d_n^4} \right]. \qquad (28)$$

3) If $\hat{k}_{ts} < -1$, the expression for the denominator is

$$D = C \left[1 - 16\frac{4L^4\lambda^4}{d_0^4} \right] \prod_{n=1}^{\infty} \left[1 + \frac{L^4\lambda^4}{d_n^4} \right]. \qquad (29)$$

In (27), (28) and (29), $C = 8EI(1+\hat{k}_{ts})$, d_n is the infinite sequence of increasingly ordered real positive solutions of the transcendental equation

$$\begin{aligned} \frac{3\hat{k}_{ts}}{d_n^3}&\left[\sinh d_n \cos d_n - \cosh d_n \sin d_n\right] \\ &= 1 + \cos d_n \cosh d_n, \end{aligned} \qquad (30)$$

and d_0 is the only positive real solution of the equation

$$2 + \cos d_0 + \cosh d_0 = -\frac{12\hat{k}_{ts}}{d_0^3}\left[\sinh d_0 - \sin d_0\right]. \qquad (31)$$

Note that C, d_n and d_0 are all parameterized by $\hat{k}_{ts}$.

Substituting $\lambda(s)$ from (14) in expressions (27)–(29), it is possible to find the location of the poles for all three cases.

For all values of $\hat{k}_{ts}$, there are poles verifying

$$\frac{cs_{\text{poles}} + ms_{\text{poles}}^2}{EI} = -\frac{d_n^4}{L^4}, \qquad (32)$$

and solving for s_{poles},

$$s_{\text{poles}} = \frac{-c \pm \sqrt{c^2 - \frac{4mEId_n^4}{L^4}}}{2m}, \qquad (33)$$
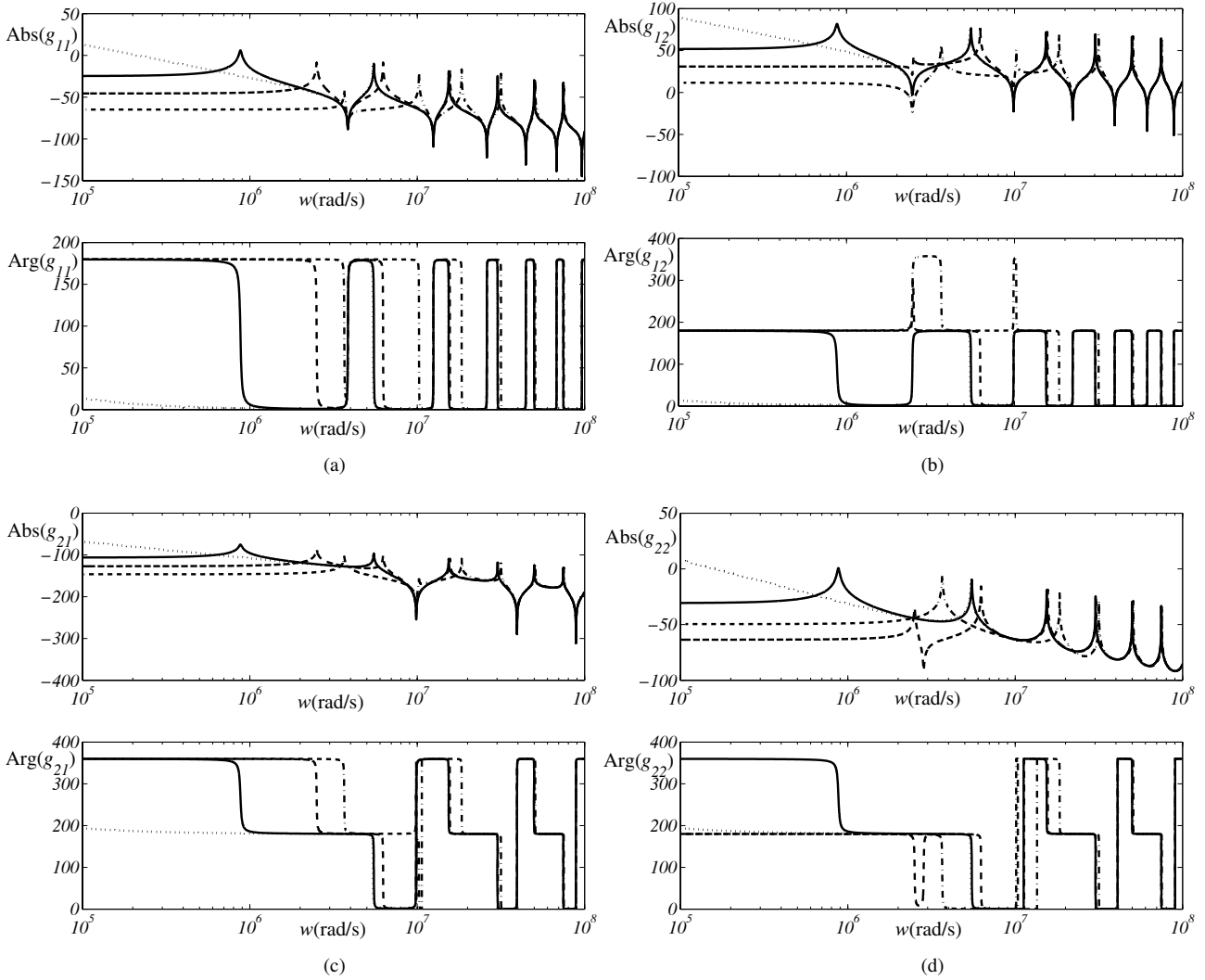
Fig. 1. Bode plots of g_{11}(a), g_{12}(b), g_{21}(c) and g_{22}(d) for $\hat{k}_{ts} = -1, 0, 10, 100$ (respectively dotted, solid, dashed and dash-dotted lines).

which, for c smaller than d_n, yields a pair of complex conjugated roots. Neglecting c, one has

$$s_{\text{poles}} \approx \pm i \frac{d_n^2}{L^2} \sqrt{\frac{EI}{m}}, \qquad (34)$$

whose modulus is a good approximation[2] to resonant frequencies.

For Case 2, in addition to the poles given by (33), there is one additional pole at the origin, and another at $-c/m$.

In Case 3, in addition to the poles in (33), there are two real poles, one with negative real part and another with positive real part (unstable pole), which are give by

$$s_{\text{poles}} = \frac{-c \pm \sqrt{c^2 + \frac{mEId_0^4}{L^4}}}{2m}. \qquad (35)$$

For the limit cases, the expressions are the following:

[2]This approximation is not valid in Case 1 for the first pair of poles, if $\hat{k}_{ts}$ is close to -1. Then d_1 approaches zero and is of the order of c, so (33) must be used.

- If $\hat{k}_{ts} = 0$, one gets the well known expression of the freely oscillating cantilever poles

$$D^0 = 8EI \prod_{n=1}^{\infty} \left[1 + \frac{4L^4\lambda^4}{b_n^4} \right], \qquad (36)$$

where b_n are the positive solutions of the equation

$$1 + \cos b_n \cosh b_n = 0, \qquad (37)$$

and the exact value of the poles is

$$s_{\text{poles}}^0 = \frac{-c \pm \sqrt{c^2 - \frac{4mEIb_n^4}{L^4}}}{2m}, \qquad (38)$$

which yields pairs of (stable) complex conjugate poles.

- For $\hat{k}_{ts} \to \infty$, the denominator (25) simplifies to

$$D^{\infty} = \frac{16EI}{3} \prod_{n=1}^{\infty} \left[1 + \frac{4L^4\lambda^4}{c_n} \right], \qquad (39)$$

where c_n are the positive real solutions of
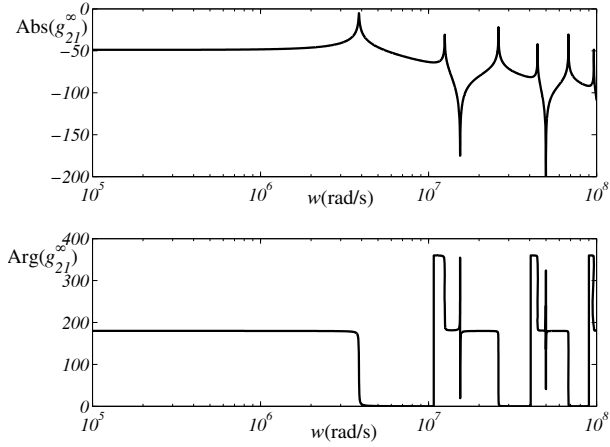
$$\tan c_n = \tanh c_n, \qquad (40)$$

Fig. 2. Bode plot of g_{22}^∞.

and the exact value of the poles is

$$s_{\text{poles}}^\infty = \frac{-c \pm \sqrt{c^2 - \frac{4mEIc_n^4}{L^4}}}{2m}, \qquad (41)$$

which yields pairs of LHP complex conjugate poles.

Using the numerical values given at the end of Section IV, we plot the poles in Fig. 3 showing how the location of the poles is altered by changing $\hat{k}_{ts}$.

The poles for the limit cases alternate on a line parallel to the imaginary axis, located on the LHP. When $\hat{k}_{ts}$ increases from zero to infinity, the poles for $\hat{k}_{ts} = 0$ (circles in the diagram) increase their imaginary part, reaching in the limit the values of the case $\hat{k}_{ts} \to \infty$ (crosses).

Analogously, for decreasing $\hat{k}_{ts}$ from zero to $-\infty$, the imaginary part of the poles decreases as well. Poles for $\hat{k}_{ts} = 0$ move towards poles of the pinned end limit case, always staying in the LHP. The only exception is the first pair of poles, whose imaginary part decrease till they become real (for $\hat{k}_{ts}$ approaching -1). At $\hat{k}_{ts} = -1$ one of them is located in the origin. Decreasing $\hat{k}_{ts}$ beyond -1 moves the pole further into the RHP, making the system unstable. This unstable behavior for the range $\hat{k}_{ts} \in (-\infty, -1)$ (strongly attractive regime of the surface coupling force) corresponds to the physical phenomena known as "snap-in" [8]. When approaching the surface closely the cantilever can, suddenly, bend towards the surface due to the attractive van der Waals forces. The instability is stopped in the real nonlinear system, since the coupling force changes sign and becomes repulsive.

VII. ZEROS

The zeros are the roots of the numerators (17)–(20). For the numerators n_{11}, n_{12}, and n_{12}, the value of $\hat{k}_{ts}$ does not change the location of zeros. We refer to [13] for a detailed study. Here, we consider only n_{22}. There are two cases.

1) If $\hat{k}_{ts} \neq -8$, n_{22} can be expanded as

$$n_{22} = -\frac{L^3}{6}(8 - \hat{k}_{ts}) \prod_{n=1}^{\infty} \left[1 - \frac{L^4\lambda^4}{z_n^4}\right]. \quad (42)$$
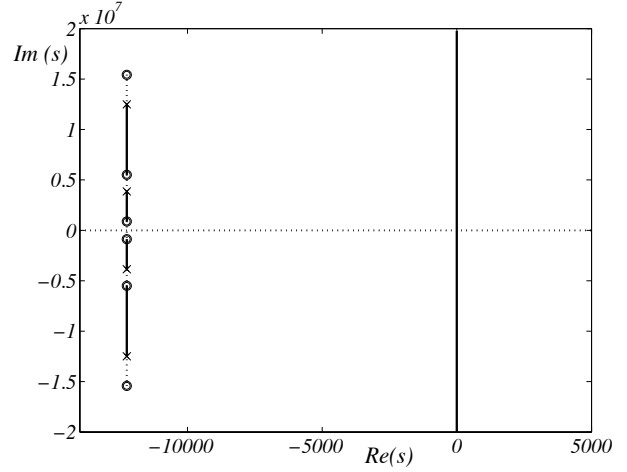

Fig. 3. Location of poles with $\hat{k}_{ts}$. Circles mark poles at $\hat{k}_{ts} = 0$, crosses at $\hat{k}_{ts} \to \infty$. Solid lines and dotted lines describe, respectively, the movement of poles for positive and negative $\hat{k}_{ts}$. The dashed line is the imaginary axis.

2) If $\hat{k}_{ts} = -8$, then a root at zero must be added, so

$$n_{22}(s) = \frac{-L^7\lambda^4}{105} \prod_{n=1}^{\infty} \left[1 - \frac{L^4\lambda^4}{z_n^4}\right]. \quad (43)$$

In expressions (42) and (43), z_n is the infinite sequence of nonzero complex solutions in the first quadrant of the imaginary plane (nonnegative real part and positive imaginary part) of the complex equation

$$4z_n^3 \left(\cosh(z_n)\sin(z_n) - \sinh(z_n)\cos(z_n)\right)$$
$$= 3\hat{k}_{ts}\left(\sin(z_n) - \sinh(z_n)\right)^2. \quad (44)$$

Substituting (14) in (42) and (43), the zeros are located at

$$s_{\text{zeros}} = \frac{-c \pm \sqrt{c^2 + \frac{16mEIz_n^4}{L^4}}}{2m}, \quad (45)$$

and one can obtain, for small c and when the values of z_n from (44) are real or close to the real axis[3], approximate value of the zeros whose absolute value gives a good approximation for the location of antiresonances:

$$s_{\text{zeros}} \approx \pm i\frac{2|z_n|^2}{L^2}\sqrt{\frac{EI}{m}}. \quad (46)$$

In the special case $\hat{k}_{ts} = -8$, in addition to the zeros in (45), there is one additional pair of real zeros, one at the origin and the other at $s = -c/m$.

The limit cases can be treated analogously.

- If $\hat{k}_{ts} = 0$, then

$$n_{22}^0 = \frac{-4L^3}{3} \prod_{n=1}^{\infty} \left[1 - \frac{L^4\lambda^4}{c_n^4}\right], \quad (47)$$

where the c_n are the solutions of (40). One has then alternating zeros in the positive and negative real axis,

$$s_{\text{zeros}}^0 = \frac{-c \pm \sqrt{c^2 + \frac{16mEIc_n^4}{L^4}}}{2m}. \quad (48)$$

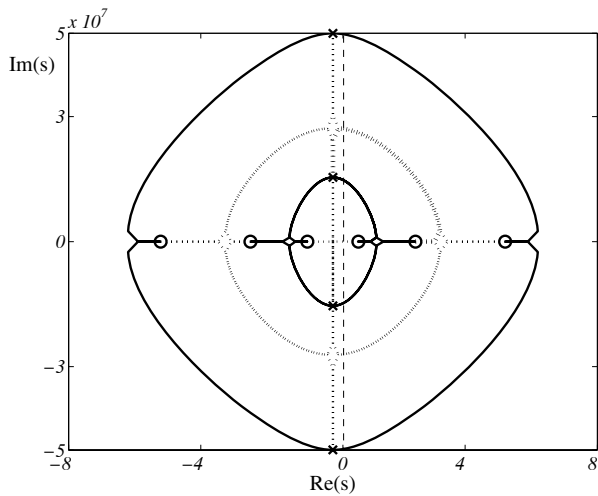[3]This situation happens for $\hat{k}_{ts}$ large, positive or negative.

536

Fig. 4. Location of zeros with $\hat{k}_{ts}$. Circles mark zeros at $\hat{k}_{ts} = 0$, crosses at $\hat{k}_{ts} \to \infty$. Solid lines and dotted lines describe, respectively, the movement of zeros for positive and negative $\hat{k}_{ts}$. The dashed line is the imaginary axis.

In this case, subsystem 22 is non-minimum phase.

- If $\hat{k}_{ts} \to \infty$, then

$$n_{22}^{\infty} = -\frac{L^3}{6} \prod_{n=1}^{\infty} \left[1 + \frac{L^4 \lambda^4}{c_n^4} \right]^2, \qquad (49)$$

where the c_n are defined in (40). The zeros have then multiplicity two, and are given by the expression

$$s_{\text{zeros}}^{\infty} = \frac{-c \pm \sqrt{c^2 - \frac{16 m E I c_n^4}{L^4}}}{2m}. \qquad (50)$$

The zeros appear in complex conjugate pairs, of multiplicity two, with negative real part, so the subsystem is minimum phase in this case.

In Fig. 4 we represent the location of the zeros of subsytem 22 when $\hat{k}_{ts}$ changes. The diagram shows the rather complex zero dynamics for different values of $\hat{k}_{ts}$.

The most interesting qualitative feature of Fig. 4 is how subsystem 22 changes from pairs of zeros in the real axis (alternatingly positive and negative) at $\hat{k}_{ts} = 0$ (circles in the diagram), to a situation in which there are pairs of complex conjugate zeros located in the LHP, for $\hat{k}_{ts} \to \pm\infty$ (crosses in the diagram). Numerically studying this behavior for intermediate values of $\hat{k}_{ts}$, we found that the approximate range $\hat{k}_{ts} \in [-14, 17]$ produces *at least some* RHP zeros, i.e. the subsystem 22 (distributed force to slope measurement) is non-minimum phase. Otherwise *all* zeros lie in the LHP, i.e., the subsystem is minimum phase.

VIII. Conclusions

In this work we have presented a systems-theoretic exact approach to study the dynamics of a surface coupled vibrating AFM cantilever, which does not neglect the infinite dimensional character of the system. Various possible inputs and outputs were simultaneously considered, and Bode plots and "root locus"-type diagrams shown. Our approach shows significant effects that simpler models cannot capture, like

non-minimum phase behavior, unstable dynamics, or variations in frequency response due to shifts of the resonant frequencies and pole-zero cancellations.

Our work opens the possibility of accurate model-based control and observer design for AFM cantilevers, to improve state-of-the-art performance in microscopy and nanomanipulation.

References

[1] N.A. Burnham, G. Gremaud, A.J. Kulik, P.J. Gallo and F. Oulevey, "Materials' properties measurements: choosing the optimal scanning probe microscope configuration", *Journal of Vacuum Science and Technology B*,vol. 14, pp. 1308–1312,1996.

[2] G. Binnig, C.F. Quate, and C. Gerber, "Atomic force microscopy," *Physical Review Letters*, vol. 56, no. 9, pp. 930–933, 1986.

[3] B. Cappella and G. Dietler, "Force-distance curves by atomic force microscopy," *Surface Science Reports*, vol. 34, pp. 1–104, 1999.

[4] R.J. Colton, A. Engel, J.E. Frommer, H.E. Gaub, A. Gewirth, R. Guckenberger, J. Rabe, W.M. Heckl and B. Parkinson, *Procedures in Scanning Probe Microscopies*, John Wiley and Sons, Chichester, 1998

[5] D.W. Dareing, T. Thundat, J. Sangmin, M. Nicholson, "Modal analysis of microcantilever sensors with enviromental damping," *Journal of Applied Physics*, vol. 97, no. 8, 084902, 2005.

[6] E.L. Florin, M. Radmacher, B. Fleck and H.E. Gaub, "Atomic force microscope with magnetic force modulation," *Review of Scientific Instruments*, vol. 65, no. 3, pp. 639–643, 1994.

[7] R.E. Goodson, "Distributed system simulation using infinite product expansions," *Simulation*, vol. 15, no. 6, pp. 255–263, 1970.

[8] H.O. Hao, A.M. Baro and J.J. Sanz, "Electrostatic and contact forces in force microscopy," *Journal of Vacuum Science and Technology B*, vol. 9, pp. 1323–1328, 1991.

[9] S. Hirsekorn, "Transfer of mechanical vibrations from a sample to an AFM-cantilever— a theoretical description," *Applied Physics A*, vol. 66, pp. S249–S254, 1998.

[10] G. Meyer and N.M. Amer, "Optical-beam-deflection atomic force microscopy: the NaCl (001) surface," *Applied Physics Letters*, vol. 56, no. 21, pp. 2100–2101, 1990.

[11] U. Rabe, K. Janser and W. Arnold, "Vibrations of free and surface-coupled atomic force microscope cantilevers: theory and experiment," *Review of Scientific Instruments*, vol. 67, no. 9, pp. 3281–3293, 1996.

[12] F.-J. Rubio-Sierra, W.M. Heckl and R.W. Stark, "Nanomanipulation by atomic force microscopy," *Advanced Engineering Materials*, vol. 7, no. 4, pp. 193–196, 2005

[13] F.-J. Rubio-Sierra, R. Vazquez and R.W. Stark, "Transfer function analysis of atomic force microscope cantilevers," accepted for publication, *Proceedings of IMECE*, Orlando, 2005.

[14] D. Rugar, H.J. Mamin, R. Erdlandsson, J.E. Stern and B.D. Terris, "Force microscope using a fiber-optic displacement sensor," *Review of Scientific Instruments*, vol. 59, no. 11, pp. 2337–2340, 1988.

[15] D.R. Sahoo, A. Sebastian and M.V. Salapaka, "Transient-signal-based sample-detection in atomic force microscopy," *Applied Physics Letters*, vol. 83, no. 26, pp. 5521–5523, 2003.

[16] V.A. Spector and H. Flashner, "Modeling and design implication of noncollocated control in flexible systems," *ASME Journal of Dynamic Systems, Measurement and Control*, vol. 112, no. 2, pp. 186–193, 1990.

[17] R.W. Stark, G. Schitter, M. Stark and R. Guckenberger, "State space model of freely vibrating and surface-coupled cantilever dynamics in atomic force microscopy," *Phys. Rev. B*, vol. 69, no. 8, 085412, 2004.

[18] D. Wouters and U.S. Schubert, "Nanolitography and nanochemistry: probe-related patterning rechniques and chemical modification for nanometer-sized," *Angewandte Chemie International Edition*, vol. 43, no. 19, pp. 2480–2495, 2004.

[19] C.A.J. Putman, K.O.V. der Werft, B.G.D. Grooth, N.F.V. Hulst and J. Greva, "Tapping mode atomic force microscopy in liquid," *Applied physics letters*, vol. 64, no. 18, pp. 2454–2456, 1994.